Seismic anisotropy and mantle flow below subducting slabs

Jack Walpole[a], James Wookey[a], J-Michael Kendall[a], T-Guy Masters[b]

[a] *School of Earth Sciences, University of Bristol, Wills Memorial Building, Queens Road, Bristol BS8 1RJ, UK*

[b] *IGPP, Scripps Institution of Oceanography, 9500 Gilman Drive, La Jolla, California 92093, USA*

Abstract

Subduction is integral to mantle convection and plate tectonics, yet the role of the subslab mantle in this process is poorly understood. Some propose that decoupling from the slab permits widespread trench parallel flow in the subslab mantle, although the geodynamical feasibility of this has been questioned. Here, we use the source-side shear wave splitting technique to probe anisotropy beneath subducting slabs, enabling us to test petrofabric models and constrain the geometry of mantle fow. Our global dataset contains 6369 high quality measurements – spanning $\sim 40,000$ km of subduction zone trenches – over the complete range of available source depths (4 to 687 km) – and a large range of angles in the slab reference frame. We find that anisotropy in the subslab mantle is well characterised by tilted transverse isotropy with a slow-symmetry-axis pointing normal to the plane of the slab. This appears incompatible with purely trench-parallel flow models. On the other hand it is compatible with the idea that the asthenosphere is tilted and

Email address: `jack.walpole@bristol.ac.uk` (Jack Walpole)

Preprint submitted to Earth and Planetary Science Letters *January 10, 2017*

entrained during subduction. Trench parallel measurements are most commonly associated with shallow events (source depth $< 50\,\mathrm{km}$) – suggesting a separate region of anisotropy in the lithospheric slab. This may correspond to the shape preferred orientation of cracks, fractures, and faults opened by slab bending. Meanwhile the deepest events probe the upper lower mantle where splitting is found to be consistent with deformed bridgmanite.
Keywords: Subduction, Seismic Anisotropy, Mantle Convection, Shear Wave Splitting, Trench Parallel Flow, Asthenosphere

1. Introduction

Subduction is an important component of mantle convection and is a prerequisite for plate tectonics; yet many dynamical aspects of subduction are not well understood (e.g., Kincaid, 1995; Bercovici, 2003; Billen, 2008; Becker and Faccenna, 2009; Alisic et al., 2012). Studying anisotropy offers a key to improve understanding in this area by linking observations from seismology to experimental and theoretically determined models from mineralogy and geodynamics.

One example of a gap in knowledge is the degree of viscous coupling between the lithospheric slab and the underlying asthenospheric mantle. The asthenosphere may be strongly coupled to the lithosphere resulting in its entrainment upon subduction (Ribe, 1989) or may be largely decoupled if it is positively buoyant (Phipps Morgan et al., 2007). This has major implications for the chemical and thermal evolution of our planet.

The idea that the asthenosphere is decoupled and flows laterally along strike at subduction zones (trench-parallel flow) has been popularised by the observations of two independent and orthogonally polarised shear waves with the faster travelling shear wave being polarised parallel to subduction zone trenches (e.g., Russo and Silver, 1994; Long and Silver, 2009). This signal fits an anisotropic model of olivine A-type fabric (or similar) with a fast polarisation direction (ϕ) that matches the flow direction (e.g., Savage, 1999, and references therein). However, even if the asthenosphere is decoupled from the slab (a mechanism for which remains elusive), it does not follow that it would flow parallel to the trench. Despite successes in modelling toroidal flow patterns at slab edges (that correlate well with shear wave splitting patterns; Kincaid and Griffiths, 2003; Civello, 2004; Zandt and Humphreys, 2008; Honda, 2009; Faccenda and Capitanio, 2012) it has proven difficult for geodynamicists to model broad scale trench-parallel flow beneath the slab using realistic parameters (e.g., Alisic et al., 2012; Lowman et al., 2007). Under realistic 3-D slab geometries the dominant flow direction is found to be normal to the trench (Kincaid and Griffiths, 2003; Alisic et al., 2012); only under special circumstances has trench-parallel flow been modelled (Lowman et al., 2007; Paczkowski et al., 2014).

The difficulty in modelling trench-parallel flow has prompted a number of alternate hypotheses to explain the splitting data; these exploit the fact that ϕ does not always equate with the mantle flow direction (e.g., Savage, 1999, and references therein). For example, under simple shear deformation, olivine B-type fabrics have ϕ normal to flow (e.g., Jung et al., 2006), leading to the suggestion of B-type fabric in the sub-slab mantle (Jung et al., 2009; Ohuchi et al., 2011; Lee and Jung, 2015). The relationship between flow and ϕ also depends on the geometry of deformation (e.g., simple shear *vs.*

pure shear; Ribe, 1992; Tommasi et al., 1999; Di Leo et al., 2014), for example trench-parallel ϕ could be caused by pure shear deformation (Faccenda and Capitanio, 2012; Li et al., 2014). Additionally, the tilting of established vertically transverse isotropy in the suboceanic asthenosphere (*a.k.a.* radial anisotropy; Dziewonski and Anderson, 1981; Nettles and Dziewonski, 2008) would produce trench-parallel ϕ for steeply incident rays (Song and Kawakatsu, 2012, 2013).

An alternative explanation for the trench parallel splitting signal is that it comes not from the asthenosphere but from the slab itself. Faults opened along the trench by flexure of the lithosphere may produce anisotropy by shape preferred orientation. Lattice preferred orientation of highly anisotropic hydrous phases within these faults could enhance the strength of anisotropy (Faccenda et al., 2008).

However, with growing numbers of observations it is becoming clearer that ϕ is often not trench-parallel (e.g., Lynner and Long, 2014a); such 'discrepant' observations are incompatible with the trench-parallel flow hypothesis. One possibility is that they indicate regions where the flow field deviates (e.g., Lynner and Long, 2014b). However such an explanation is unsatisfactory in regions where observations of ϕ are highly variable over short distance. Local variability in splitting parameters is potentially better explained by variation in sampling geometry depending on the symmetry properties of the anisotropic medium (e.g., Song and Kawakatsu, 2012).

In addition to the shallow sources of anisotropy, anisotropy is also thought to exist in the deeper mid-mantle (i.e., transition zone and the upper lower mantle, between about 400 to 1000 km depth). Such deep anisotropy can inform us on the dynamical processes of slab sinking into the viscous lower mantle. It also constrains mineralogical models of, for example, deep water transport (Nowacki et al., 2015). Observations of source-side splitting from deep events on downgoing S phases has provided firm evidence for anisotropy in the mid-mantle (Wookey et al., 2002; Lynner and Long, 2015; Mohiuddin et al., 2015; Nowacki et al., 2015). Anisotropy may be a global feature of the transition zone as has been inferred from surface wave data (Trampert and van Heijst, 2002; Yuan and Beghein, 2013), though some localised mid-mantle regions show an apparent lack of anisotropy (Fischer and Wiens, 1996; Fouch and Fischer, 1996; Kaneshima, 2014).

In this study we present a new dataset of source-side S shear wave splitting measurements – the largest of its kind to date – that covers $\sim 40,000\,\mathrm{km}$ of the Earth's subduction zones. The dataset includes shallow and deep events enabling us to probe anisotropy in the shallow and deep mantle. This is enabled by automation of the analysis supported by newly developed quality control measures (such as for robust null detection and consideration of error) and manual verification. We analyse the variation in splitting parameters with sampling angle in the slab reference frame in order to expose the underlying character of anisotropy.

2. Data and Methods

2.1. Seismic Data Selection

We use the source-side splitting technique (e.g., Kaneshima and Silver, 1992; Vinnik and Kind, 1993; Wookey et al., 2002; Nowacki et al., 2012; Di Leo et al., 2012; Lynner and Long, 2013) to probe anisotropy in the region directly beneath earthquake hypocentres (therefore these data have no sensitivity to the overlying mantle wedge); the concentration of seismicity at convergent plate boundaries makes this technique ideal for studying anisotropy in the sub-slab mantle. We use the catalogue of data available on the Fast Archive Recovery Method (FARM) volumes provided by the Incorporated Research Institutions for Seismology (IRIS) Data Management Center (DMC). The data cover the years from 1976 to 2010, incorporating all events in magnitude range $4.0 \leq M_w \leq 7.3$. Clear S arrivals are picked using a hierarchical clustering technique on long-period data (Houser et al., 2008). We select data within the epicentral distance window $50° \leq \Delta \leq 85°$; at shorter distances S phases arrive at stations with shallow incidence angles where free-surface coupling effects and shear-coupled P waves can distort the particle motion (e.g., Wookey and Kendall, 2004); at farther distances the signal is potentially contamination by splitting in the lowermost mantle (e.g., Wookey et al., 2005; Wookey and Kendall, 2008). In total, data from 4955 events and 1903 stations are used to measure source-side splitting on 64,333 raypaths (Fig 1); however quality control eventually reduces this number to 6369 high quality measurements sourced at subduction zones; only these latter measurements will be considered in this study.

2.2. Measuring Shear Wave Splitting

Shear wave splitting is measured using the semi-automated workflow described in Walpole et al. (2014) adapted for the source-side splitting technique. Prior to measurement, the data are Butterworth bandpass filtered to pass signal in the frequency range $0.02-0.30$ Hz. The phase pick times are used to determine time window limits for particle motion analysis; the final

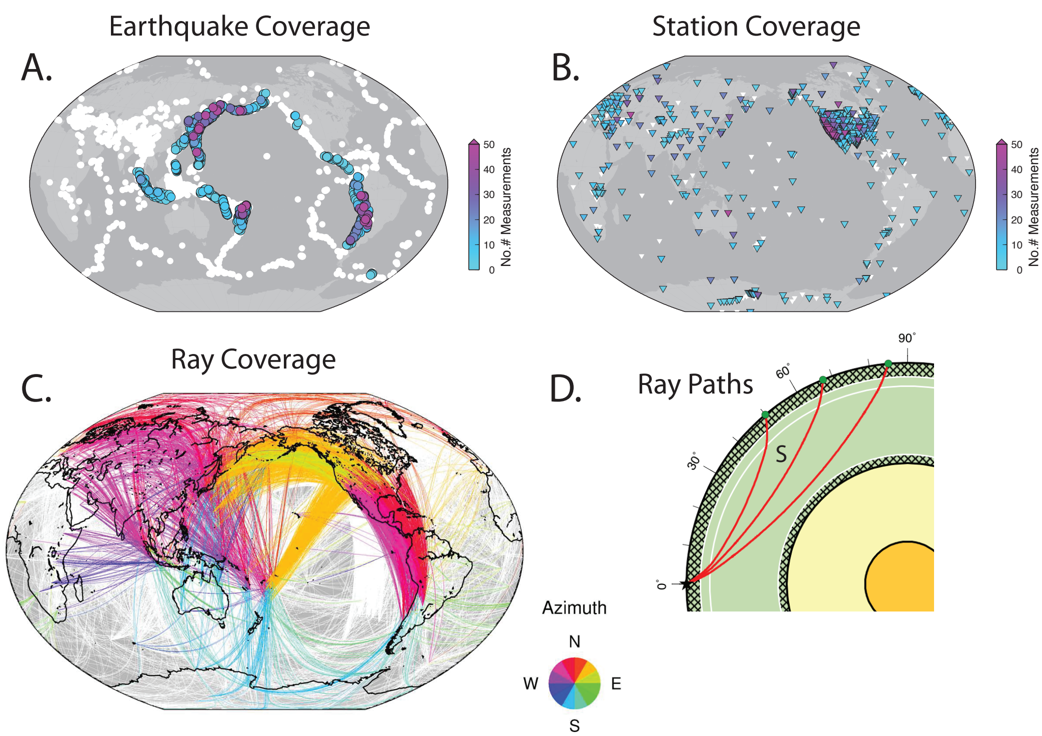

Figure 1: Maps of **A.** earthquake events; **B.** seismic stations; **C.** raypaths. In each of these colour is used to denote events/stations/raypaths associated with high quality source-side splitting measurements at subduction zone locations. Note that many measurements are rejected based on quality or simply discarded based on location; these are shown by the white symbols. **D.** Cross-sectional view of the Earth with S paths shown for epicentral distances 50° to 85° (the range used in the dataset); the upper mantle and lowermost mantle region are hatched to denote that these regions are anisotropic.

window is selected by a clustering algorithm that searches for the window that returns the most stable result (Teanby et al., 2004; Wuestefeld et al., 2010). Splitting is measured using both the minimum eigenvalue method (Silver and Chan, 1991) and the cross-correlation method (Ando et al., 1980). The use of both techniques tests whether a result depends on the measurement method (Wuestefeld and Bokelmann, 2007), the degree to which the methods agree is quantified by the Q parameter (Wuestefeld et al., 2010). In this study we present the results obtained by the minimum eigenvalue method, along with the parameter Q.

2.2.1. Receiver Correction

Since S phases pass through the anisotropic upper mantle twice (downwards in the source region, and upwards in the receiver region, Fig 1 D), the observed split shear wave must be corrected for splitting in the receiver region before the source-side splitting can be measured. In principle the shear-wave could split due to anisotropy along its lower mantle path, however, evidence suggests that the bulk of the lower mantle is isotropic (e.g., Meade et al., 1995; Panning and Romanowicz, 2006) and therefore should not contribute significant splitting. Splitting that does occur in the lower mantle will interfere and add variance to our measurements; however a consistent signal in the source region should dominate the average over many measurements.

Knowledge of the receiver correction is constrained by splitting measured on SKS and $SKKS$ phases, which are radially polarised (SV) by a P to S conversion at the core-mantle boundary, and therefore only retain a splitting signal from their upward journey through the mantle. In general, the receiver correction depends on incidence angle, back-azimuth, polarisation, and frequency of the incoming wave and therefore $SK(K)S$ derived corrections may not be accurate for the particular S phase under study. To address this problem we devise and implement an iterative workflow to find the receiver correction for each S phase in the study individually (Fig S1). The technique improves either the receiver- or the source-side splitting parameters with each successive iteration. The initial iteration uses SKS and $SKKS$ data in conjunction with (uncorrected) S data to make a first estimate of the receiver correction (the SKS measurements are described in Walpole et al., 2014); this is achieved for each station by signal-to-noise weighted error surface stacking of all measurements at that station (Restivo and Helffrich, 1999). The second iteration applies these receiver corrections to S phases to measure the source-side splitting; in turn source-corrections are derived by signal-to-noise weighted stacking of all measurements from a common event. The third iteration uses these source corrections to make more accurate receiver-side splitting measurements on the S phases. The fourth iteration uses SKS, $SKKS$, and source-corrected S phases (from the previous iteration) to make an updated measurement of the receiver correction; however, in order to make this correction as appropriate as possible to the S phase under investigation, only phases polarised within 15° of the target S phase contribute to this receiver correction. With successive iterations the corrections become increasingly specific to the particular S phase under study. By iterations 5 and 6 the source/receiver correction is derived exclusively from the exact seismogram on which the measurement is being made, thereby accounting for possible dependence on incidence angle, back-azimuth, polarisation, and frequency. We present the results from iteration

6 in this paper, these are (receiver corrected) measurements of source-side anisotropy.

2.2.2. Propagating of Error in the Receiver Correction

Inevitably the receiver correction carries some degree of uncertainty. This renders the receiver correction an error prone process. No previous study has attempted to propagate the uncertainty in the receiver correction into the error of the final measurement. Here we introduce a new method to achieve this.

The main principle of the new method is to test numerous possible receiver corrections, and to combine the resultant measurements together into one measurement that captures the potential variability in the result. This is achieved by using a shear wave splitting error surface as the input to receiver correction (rather than the single set of splitting parameters typically used). Specifically, this error surface takes the form of an F-test normalised grid of λ_2 values, output from a minimum eigenvalue measurement (Silver and Chan, 1991), or possibly from a stack of such measurements (Wolfe and Silver, 1998). λ_2 is defined as the minimum eigenvalue of the two dimensional time-domain covariance matrix of particle motion within the polarisation plane (Silver and Chan, 1991). Each trial measurement produces its own error surface, which is weighted by the inverse of the normalised λ_2 value associated with the trial splitting parameters in the input receiver correction surface. Ultimately an ensemble of measurements is amassed, which are stacked to produce the final measurement. In principle it would be desirable to test each possible receiver correction, however, the computational cost increases by a factor of N, where N is the number of candidate receiver corrections to test. Pragmatically we limit N to 50, and use a random sampling method to select candidate corrections, the sampling method is biased towards selecting receiver corrections with low values of λ_2 (and therefore more likely to be true). The biased random selection method works as follows: for each node selection, 100 nodes are randomly sampled from the grid and only that with the minimum λ_2 from these 100 is retained for further use. This process is repeated until 50 unique nodes have been selected. Picking the "best" node from the 100 random samples biases the selection towards the most realistic receiver corrections. The size of the random subset affects the severity of the biasing; the choice of 100 samples was found, by testing, to be a reasonable subset size given the total number of nodes in our error surface ($180 \times 161 = 28,980$). A demonstration of the error propagating receiver correction method as applied to synthetic data is provided in Figure S2.

2.3. Null Classification

The classification of measurements as *split* or *null* is important for interpretation. A new metric for automatic null classification is employed. This metric, here named "Null Intensity" (NI), uses a 2-D normalized cross-correlation of the error surface with itself (autocorrelation) to search for self-similarity at 90° offset in ϕ. Autocorrelation is facilitated by expanding the error surface by wrapping around the ϕ axis and mapping into negative δt as demonstrated in Figure S3. The method exploits 90° ambiguity in ϕ that is characteristic of null measurements: the essential idea is to look for strong autocorrelation at 90° misfit as evidence for a null measurement. Testing has revealed that taking a second autocorrelation leads to a more stable metric for null identification, because it enhances the separation between *null* and *split* measurements. The value of NI is here defined as the value at 90° misfit of the second autocorrelation of an error surface. The value varies between -1 and +1, where values of +1 indicate a perfect *null* measurement. Examples of this method applied to *null* and *split* measurements are provided in Figs S4 and S5. Further details of this method are contained in the Supplementary Materials. A comparison with the Q method of Wuestefeld et al. (2010) is provided in Figure S6. Testing on the random subset of data reveals that values of NI less than about +0.8 tend to be *split*. Combining the NI metric with the Q value of Wuestefeld et al. (2010) greatly improves our automated *null*/*split* classification. We automatically classify any measurement with $NI > 0.8$ and $Q \leq -0.75$ as *null*, and any measurement with $NI \leq 0.8$ and $Q > -0.75$ as *split*.

3. Final data selection

Manually verified quality control (QC) is applied to both the source-side (iteration 6) and receiver-side (iteration 5) datasets to filter out low quality measurements. Automatic null and split classification is also applied to aid in interpretation. The details of these processes are described in the Supplementary Materials and the success rate is examined in Figure S7.

To ensure that measurements are made using good receiver corrections, source-side measurements are excluded if the corresponding receiver-side measurement fails the QC procedure. The source-side dataset contains 64,333 measurements of which 13,781 (21%) pass QC with "good" receiver correction. Of these: 6632 (48%) are automatically classified as *split*, 5106 (37%) are automatically classified as *null*, and 2043 (15%) are unidentified. Histograms of many useful measurement statistics (e.g., signal to noise ratio) are shown in Figure S8.

To further reduce the dataset to the best measurements we discard *split* data with errors $\sigma_\phi > 15°$ and $\sigma_{\delta t} > 0.3$ s and *null* data with $\sigma_\phi > 15°$; this reduces the number of measurements to 7819. For the purposes of concentrating our attention on subduction zones we further discard data from sources not colocated with a slab (according to the model Slab1.0; Hayes et al., 2012); this reduces the final dataset down to 6369 splitting measurements to be examined in this study (coverage shown in Figure 1).

4. Results

4.1. Delay Times

Delay times (δt) measure a combination of anisotropy strength and path length through the anisotropic region. Figure 2 A shows the variation in δt with depth for all *split* (non-null) measurements.

To first order δt values decline with source depth (Fig 2 A). Median δt, hereafter $\widetilde{\delta t}$, drops from 1.7 s in the 0–50 km depth bin to 1.3 s in the 200–250 km depth bin: a decrease of 0.4 s over a depth change of 200 km. This drop is strong evidence for the presence of anisotropy above 200 km. One could explain 1.7 s of splitting by a 380 km path length through a region of 2% anisotropy (though due to the tradeoff of path length with anisotropy strength other solutions are possible, e.g., 260 km through a region of 3%). Assuming a simple dipping layer geometry this would correspond to a layer thickness of about 290 km (or 200 km with 3% anisotropy). This calculation assumes that rays propagate along a path $\sim 40°$ incident from the slab

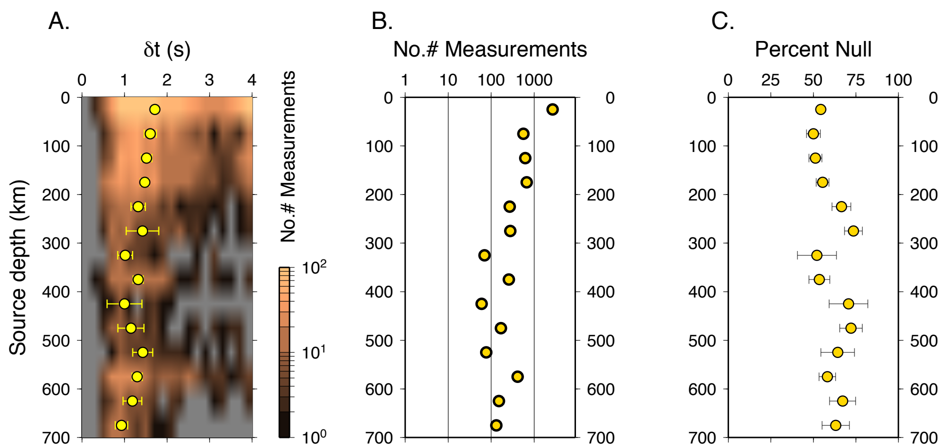

Figure 2: **A.** Global 2-D histogram of *split* measurement delay times, δt, against source depth in 0.2 s by 50 km bins; median δt symbols plotted on top with 95% confidence intervals calculated by bootstrapping. Copper colours show the number of measurements within a bin according to the inset logarithmic colour scale; grey background colour indicates no measurement within bin. **B.** Total number of measurements – *split* and *null* – for each depth. **C.** Percentage of *null* measurements for each depth with 95% confidence intervals calculated by bootstrapping.

normal vector, which is typical within the dataset. The smooth decrease in $\widetilde{\delta t}$ with depth indicates either a gradual shortening of the path length (e.g., due to thinning of the layer) or weakening of anisotropy with depth. To explain 1.3 s of splitting from sources in the depth range 200–250 km requires a path length of 290 km through 2% anisotropy (or a path length of 200 km through 3% anisotropy). Given a dipping layer this corresponds to inferred layer thicknesses of 225 km and 150 km in the cases of 2% and 3% anisotropy respectively. Therefore, in the scenario that the anisotropic region is a dipping layer with strength 2% throughout, the layer thins from 290 km near the surface to 225 km beneath $\sim$ 200 km depth.

To within 95% confidence $\widetilde{\delta t} \sim 1.3$ s over the entire depth range 200–600 km. This agrees with results reported in several recent studies employing similar methodology (Lynner and Long, 2015; Nowacki et al., 2015; Mohiuddin et al., 2015). The apparent lack of depth dependence might indicate the mantle is isotropic over this depth range and that all splitting shares a common anisotropic source in the deeper mantle. However, observations from surface waves, which have good depth resolution, indicate that the transition zone (410–660 km) is globally anisotropic with a detectable azimuthal component (Trampert and van Heijst, 2002; Yuan and Beghein, 2013). Therefore the lack of depth dependence on $\widetilde{\delta t}$ may require a more complex interpretation than simple isotropy. One possibility is that anisotropy is present throughout the depth range 200–600 km but that interference in the splitting signal from multiple regions of anisotropy conspires to produce no apparent depth variation in $\widetilde{\delta t}$.

The detection of splitting on the deepest events (deeper than 650 km) is strong evidence for the presence of anisotropy in the upper lower mantle. Splitting delay times of $\sim 1\,\mathrm{s}$ require a path length of 300 km through a region with 2% anisotropy; assuming a dipping layer geometry such a layer would need to be about 180 km thick. This calculation assumes that rays propagate along a path $\sim 50°$ incident from the slab normal vector, which is representative of our data at this depth.

4.2. Fast Directions

Previous observations of trench parallel fast directions have been used to support the sub-slab asthenospheric trench parallel flow hypothesis (Russo and Silver, 1994; Long and Silver, 2008, 2009). Figure 3 A shows the global distribution in the fast wave polarisation direction as projected in the geographical reference frame at source location (ϕ_{src}, measured in degrees clockwise from north) coloured by misfit from the local strike of the subducting slab (using model Slab1.0; Hayes et al., 2012). There is a large degree of local variability in ϕ_{src} (e.g., in the South American and Japan-Kuril subduction systems, Fig 3 A) demonstrating that trench parallel fast directions are far from ubiquitous, though they are slightly more prominent than non-trench-parallel observations (Fig 3 B). Variability has previously been attributed to heterogeneity in the sub-slab mantle or systematic variations due to ray azimuth and takeoff angles relative to the dip and strike of the slab caused by the style of anisotropy (Song and Kawakatsu, 2012). It is worth noting that the number of trench parallel observations is increased significantly if only considering events sourced in the upper 50 km (Fig S9).

Regional plots of each subduction zone considered in this study are presented in supplementary figures S10 – S19. These plots show the geographical

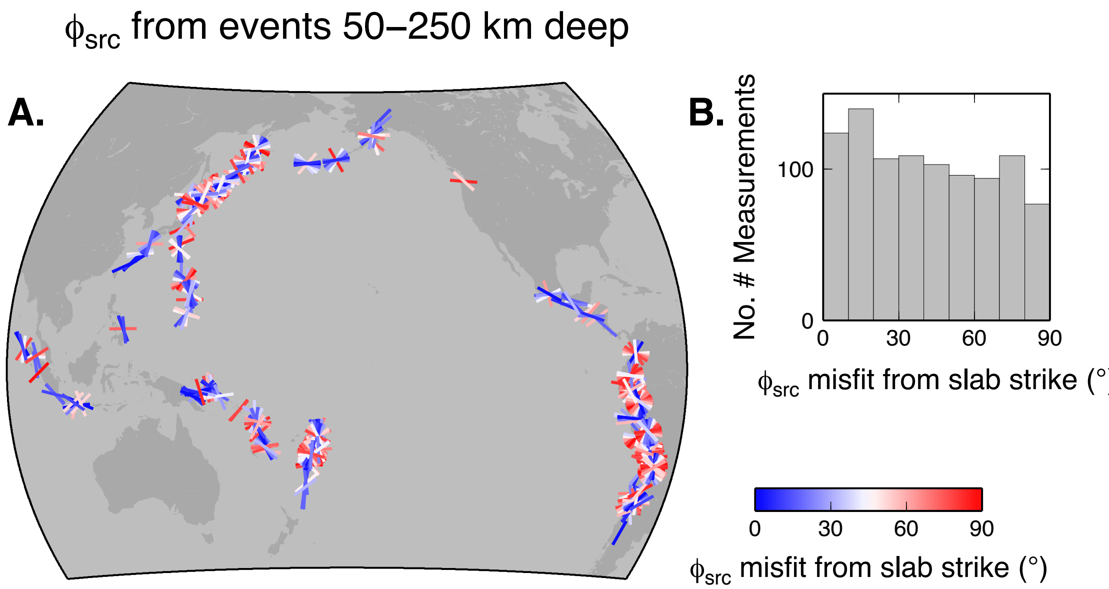

Figure 3: **A.** Map of ϕ_{src} measurements from sources in the depth range 50–250 km; coloured by misfit from slab strike parallel (approximately trench parallel): blue symbols are parallel – and red symbols normal – to strike. **B.** Histogram of ϕ_{src} misfit from slab strike parallel. Despite a large degree of variation, strike parallel measurements are slightly more frequent than any other measured orientation. Orientations in the source frame are calculated according to the equation: $\phi_{src} = \alpha + \beta - \phi_{rcv}$; where α is azimuth, β is back azimuth, and ϕ_{rcv} is the fast direction, measured clockwise from north, at the seismic station.

distribution of measurements projected into the source reference frame with ϕ_{src} measured from geographical north. This projection assumes a vertical ray and therefore does not capture variability with takeoff angle or azimuth. In order to demonstrate such variability the source frame maps are accompanied by polar panels showing the measurements separated by azimuth and takeoff angle and the fast direction measured from the projection of the vertical direction on the sphere, ϕ_{ray} (vertically polarised 'SV' waves have $\phi_{ray} = 0°$ and correspond to radial lines on these plots).

To investigate the possibility that splitting varies systematically with sampling geometry in a globally consistent way we use the slab reference frame (Nowacki et al., 2015). This reference frame accounts for variations in the ray path in relation to the dip and strike of the subducting slab providing a convenient way to incorporate the entire global dataset into a single analysis. The slab frame has three orthogonal axes forming a right-handed co-ordinate system: strike = **1**; dip = **3**; and slab normal = **2** (Fig 4 A). Azimuths are measured clockwise from strike (**1**) and takeoff angles are measured relative to the dip vector (**3**). Note that if the slab has very shallow dip then it is possible that rays may take off at angles greater than 90° from the dip vector and hence our plots extend to incorporate takeoff angles of up to 120°. The fast direction, ϕ_{slab}, is measured relative to the projection of the slab dip vector (**3**) on the sphere. If $\phi_{slab} = 0°$ then the fast shear wave is polarised parallel to slab-dip and we will refer to these measurements as 'dip parallel' (in an analogous way to SV waves being polarised parallel to the vertical direction); if $\phi_{slab} = \pm 90°$ then the fast shear wave is polarised normal to slab-dip and we will refer to these measurements as 'dip normal' (in an analogous way to SH waves being polarised normal to the vertical direction).

Despite the predominant use of 'trench parallel' as a reference orientation for describing fast directions in the preexisting literature, we find it more useful to describe our slab frame data in terms of 'dip parallel', this is natural in the slab frame as ϕ_{slab} is measured relative to the projection of the dip vector on the sphere. In principle one could measure the fast direction in relation to the projection of the strike axis ($\mathbf{1}$) on the sphere and this would facilitate description in terms of 'trench parallel'. One can do this visually by checking that the orientation of the bar points towards the strike axis ($\mathbf{1}$); e.g., the model shown in Fig 4 C predicts trench parallel measurements at every sampling angle.

In Figure 4 B–D we show a handful of simple tilted transverse isotropy (TTI) models in the slab reference frame. These models act as simple analogues for a range of plausible anisotropic scenarios in the subslab mantle and these are discussed briefly in the figure caption. In Figure 5 a further selection of models is shown within the slab reference frame. Models H and I are relevant to anisotropy in the upper lower mantle and the lithosphere respectively. We will compare our data to these models in order to gain insight into the nature of anisotropy in the mantle beneath subduction zones.

In Figure 6 we plot the global dataset in the slab reference frame with colours used to emphasise the orientation change in the fast shear wave polarisation direction. The contribution towards the global coverage from different geographic regions is shown in the bottom row of panels in this figure. We observe that variability in the fast direction becomes systematically organised in the slab frame whereby dip normal ϕ_{slab} measurements cluster at azimuths normal to slab strike and dip perpendicular ϕ_{slab} measurements cluster at oblique azimuths. This basic pattern is seen over the full range of source depths with the exception of the deepest events where coverage at azimuths normal to slab strike is poor (Fig 6 D). It reveals a systematic globally consistent nature of anisotropy in the sub-slab mantle controlled fundamentally by the overlying slab.

To extract a global representation of this splitting pattern for a series of source depth ranges we calculate the circular mean of ϕ_{slab} and median of δt within equal area bins over the sphere (Fig 7). In doing so we assume mirror symmetry about the plane normal to strike enabling us to confine almost all sub-slab measurements to a quadrant of the hemisphere. To test hypothetical models of sub-slab anisotropy the observed pattern can be compared to the expected patterns of candidate models (i.e. compare results in Fig 7 to models in Figs 4 and 5).

4.2.1. 50 to 250 km deep sources

We primarily concentrate on data from sources 50 to 250 km deep; this range is chosen to focus on the asthenospheric sub-slab mantle whilst avoiding bias from the overwhelming number of shallow events in the dataset. In Figure 8 we show the difference in ϕ_{slab} between candidate models and our averaged representative observations over the sampled range of angles in the slab frame. The models that best replicate our ϕ_{slab} pattern are the TTI slab normal model (Fig 8 D) and the orthorhombic model of Song and Kawakatsu (2012) (Fig 8 G). The TTI slab normal model is a simple case of elliptical anisotropy, with a slow symmetry axis, defined by the Thomsen pa-

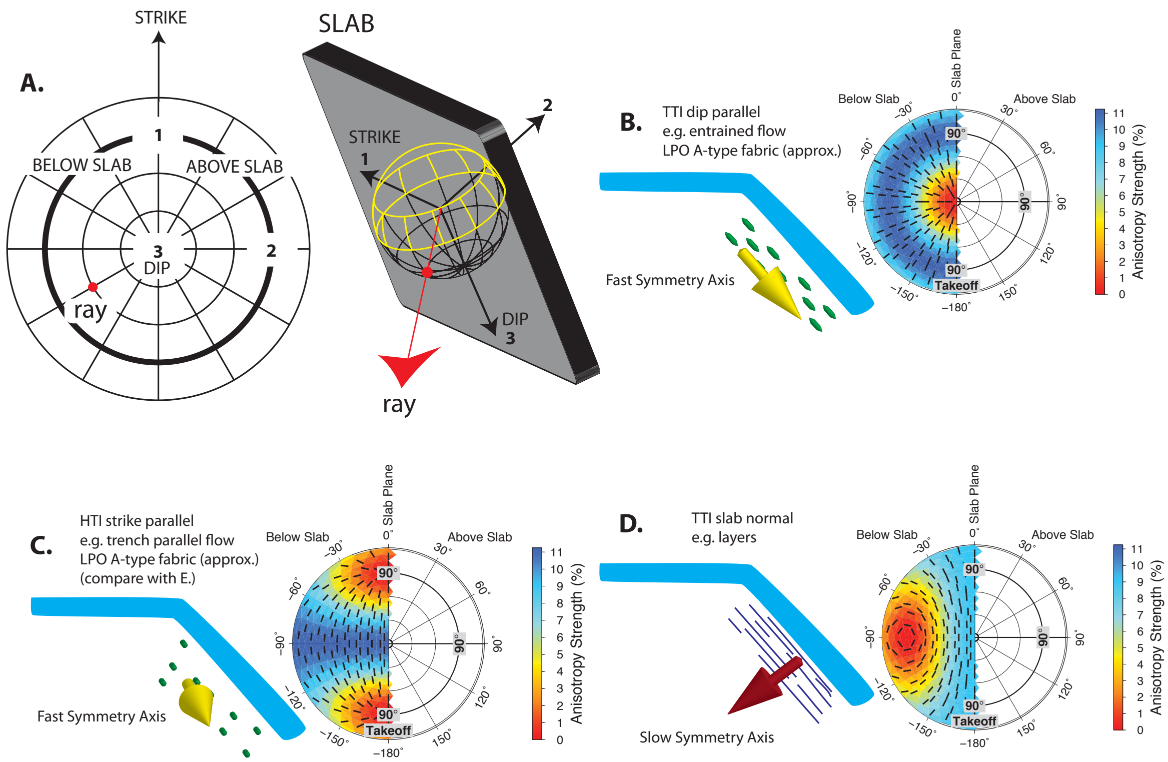

Figure 4: **A.** *(left)* Sketch of the slab reference frame projected on to a polar grid with radial direction corresponding to ray takeoff angle as measured from the dip vector (3-axis directed down into the centre of the polar grid) and tangential direction corresponding to ray azimuth as measured from the strike vector (1-axis). The region left of the vertical line that defines the plane normal to 2 (i.e. the slab plane) contains all rays that exit beneath the slab and likewise right of this line rays would exit above the slab; rays situated along this line have long slab paths. A ray taking off at 60° from the dip vector at an azimuth −120° from strike is plotted as a red dot. *(right)* Natural perspective of the slab frame (wireframe mesh) with the familiar ray this time shown as a red arrow shooting down beneath the slab. Notice that the grid extends to takeoff angles up to 120°; these angles are necessary as they are occasionally sampled in situations where the slab dip is very shallow. **B.** Demonstration of a simple tilted transverse isotropy (TTI) model with fast symmetry axis parallel to the slab dip vector. The small black bars show the fast polarisation direction ϕ_{slab} pointing radially (parallel to the symmetry axis) at all locations with colour showing that anisotropy is strongest at angles normal to the symmetry axis and weakest at angles parallel to the symmetry axis. This model is analogous to the case of olivine A-type fabric entrained by subduction. **C.** Similar to (B.) except the symmetry axis is pointing parallel to the strike vector; this case is analogous to olivine A-type fabric oriented trench parallel. **D.** Similar to (B.) and (C.) except the TTI model has a slow symmetry axis which points normal to the slab plane; this case is analogous to fine layers

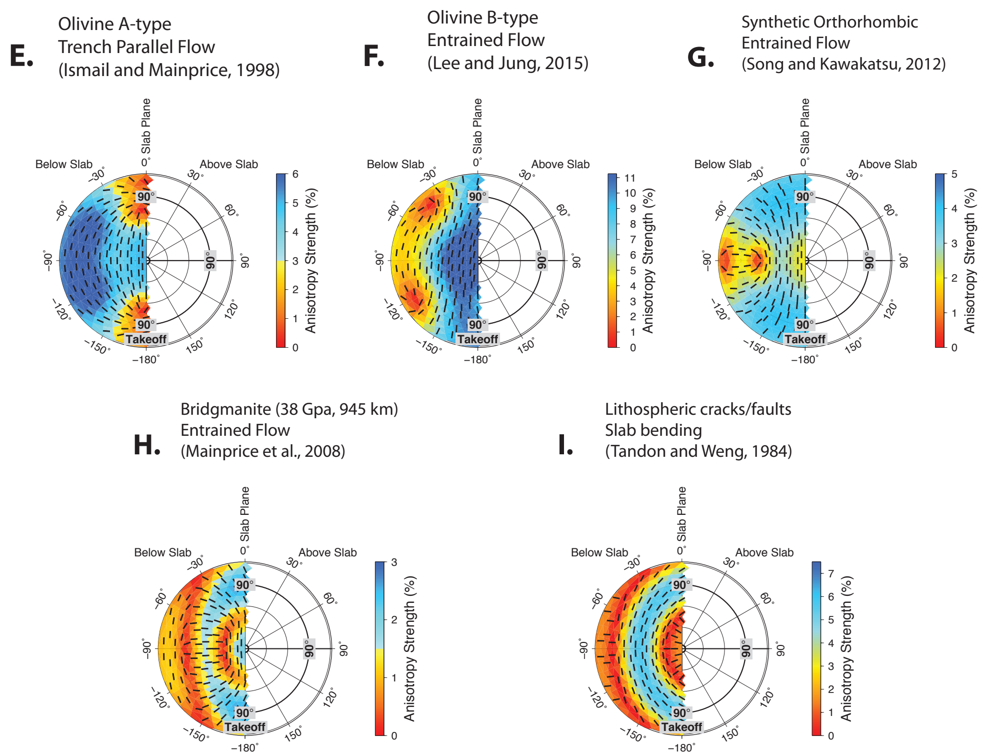

Figure 5: Selection of elastic models in the slab reference frame. **E.** A-type fabric average from a database of natural olivine fabrics (Ben Ismail and Mainprice, 1998) rotated with foliation plane parallel to the slab plane and lineation parallel to strike vector (trench parallel flow; *cf.* Fig 4 C). **F.** B-type natural olivine fabric (Lee and Jung, 2015) with foliation plane parallel to slab and lineation parallel to dip vector (entrained flow). **G.** Orthorhombic model of Song and Kawakatsu (2012) combining elements of models B and D (Fig 4). **H.** Lower mantle bridgmanite texture (Mainprice et al., 2008) rotated with foliation parallel to slab and lineation parallel to dip vector (entrained flow; crystallographic texture calculated at 30 GPa under simple shear deformation with a strain of 2.0 and single crystal elastic constants calculated at 1500 K and 38 GPa). **I.** Cracks/faults dipping at 60° within the slab (angle measured from horizontal if the slab were flat, the slab frame naturally accounts for any extra tilting of the slab); modelled using the effective medium theory of Tandon and Weng (1984). Elastic constants for all models given in supplementary Table S1.

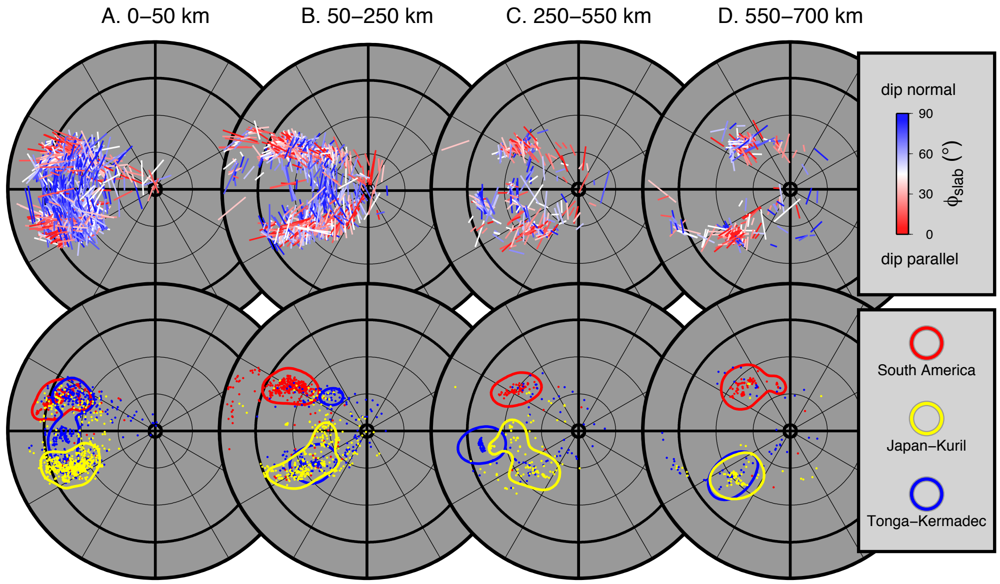

Figure 6: **Top row:** Splitting in the slab reference frame for the global dataset separated by source depth (consult Fig 4 for explanation of this reference frame). Fast direction, ϕ_{slab}, shown by orientation and colour of bar symbols. Red bars are parallel to the slab dip vector, blue bars are normal to this direction. Length of bar corresponds to δt with the longest bars equalling 4 s of splitting. We note good separation of dip normal (blue) and dip parallel (red) ϕ_{slab} measurements in this reference frame. **Bottom row:** Constitution of the global dataset broken down into three broad regions:– *red* – mainly from the South American subduction system with minor contributions from the Cascadian, Mexican, and Scotian systems;– *yellow* – mainly from the Japan-Kuril subduction system with contributions from the Izu-Bonin-Mariana, Ryukyuan, and Aleutian systems;– *blue* – mainly from the Tonga-Kermadec subduction system with contributions from the Indonesian, Philippine, Solomon, and Vanuatuan systems.

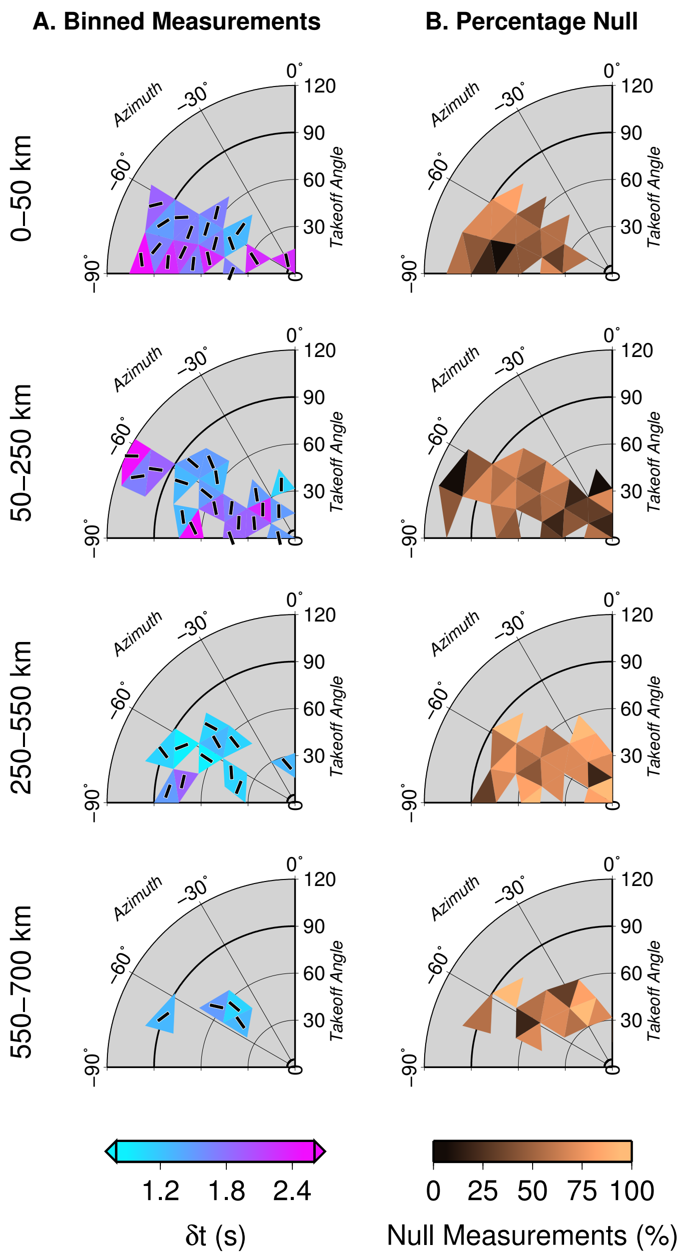

Figure 7: **A.** Averaging of the slab frame measurements shown in Figure 6. Circular mean ϕ_{slab} and median δt are calculated within equal area triangular bins for a range of source depths (indicated on the left). Only bins containing at least 4 measurements and standard errors of less than 20° in ϕ_{slab} and 0.8 s in δt (calculated by bootstrapping) are shown. **B.** Percentage of null measurements detected within each bin. Only bins containing at least 4 measurements and standard error less than 15% (calculated by bootstrapping) are shown.

rameters $\delta = \epsilon = \gamma = 0.1$ (Thomsen, 1986). The latter orthorhombic model essentially embellishes the former TTI model with a component of azimuthal anisotropy in the direction of plate movement to represent the observed azimuthal anisotropy in the asthenosphere (Song and Kawakatsu, 2012). We are not able to distinguish between these models due to a gap in coverage where the main difference would manifest (azimuth $-90°$ and takeoff angle $90°$, relative to the strike and dip vectors of the slab respectively); these angles are covered by steeply incident phases (e.g. SKS) on shallow dipping slabs (Song and Kawakatsu, 2012, 2013). Trench-parallel flow models strongly misfit the observations at azimuths $\sim -60°$ and takeoff angles $\sim 90°$ (Figs 8 C and E); similarly the entrained B-type model also misfits at these angles (Fig 8 F). This is evidence that trench parallel flow is not likely to be a dominant mode of material transport in the sub-slab mantle (the same argument rules out the entrained B-type model). By similar argument: misfit at azimuths $\sim -90°$ rules out the entrained olivine A-type model (Fig 8 B). Olivine C-type and E-type fabrics are more likely to exist in the asthenosphere than A-type fabric (Karato et al., 2008); we notice the character of the splitting pattern associated with these fabrics is qualitatively similar to A-type fabrics (Fig S21) such that they can be reasonably well approximated by hexagonal symmetry with a fast symmetry axis. Our data seem to require a slow symmetry axis and therefore C- and E-type fabrics are not compatible with our observations.

To investigate the extent to which this global observation holds in separate regions we consider the percentage of measurements that fit a given model for each subduction zone. To do this each fast direction measurement is modelled as a wrapped gaussian function (180 degree periodicity), normalised so that the area under the curve equals one, and with a width and height determined by the errors in the measurement and a peak location corresponding to the angular misfit from the model predicted fast direction. The ensemble of all measurements (i.e. gaussians) for a particular region is then stacked and renormalised so that the area under the curve is equal to one hundred. The resultant curve is a kernel density estimation (KDE; Parzen, 1962) showing the distribution in misfit between the data and the model. Such a curve can be considered as a smooth histogram. The area under the curve in the interval -30 to 30 degrees represents the percentage of measurements that fit the model (fast directions) within 30 degrees. Figure S22 shows the KDE misfit curves for a selection of the best sampled regions for both the slab normal model (left panel) and the trench parallel model (right panel). The area beneath these curves in the interval -30 to 30 degrees for each region is tabulated in Table S2.

Generally speaking the slab normal model performs better than the trench parallel model for the majority of regions as shown by the higher percentage of measurements within the $\pm 30°$ interval. This is especially true of the South American and Honshu-Kuril regions where the high number of measurements indicates statistical significance. These regions are the best sampled regions in the dataset not simply because of their high number of measurements but also because they contain ray coverage at a wide range of sampling angles. Importantly, in both these region there is sampling at the key angle around $-60°$ azimuth and $75°$ takeoff in the slab reference frame where the difference between the slab normal and trench parallel models is clearest (Fig S20). The

Tonga-Kermadec subduction zone is anomalous in that the trench parallel model appears to fit better than the slab normal model. This subduction zone is notable for strong trench roll-back in the north (from where most measurements are obtained) perhaps associated with an abnormal sub-slab mantle flow. However, though this region yields a good number of measurements, the slab frame coverage is limited at the key angles needed to most clearly distinguish between the trench parallel and slab normal models (Fig S20). In the Aleutia-Alaska, Izu-Bonin-Mariana, Ryukyu, Solomon, and Vanuatan regions the slab normal and trench parallel models perform similarly. This is not surprising as the coverage in these regions is limited to angles at which both models predict similar fast directions (Fig S20). The Philippine, Central America, Sandwich, and Indonesian regions are limited by a low number of measurements and therefore we do not comment on these.

In summary the slab normal model is clearly better than the trench parallel model beneath South America and the Honshu-Kuril subduction zones, but not beneath the Tonga-Kermadec system (though this region lacks key coverage at the most diagnostic slab frame angles). In other regions coverage is not sufficient to strongly prefer one model over the other. Therefore we *can* rule out large scale trench-parallel flow beneath the best sampled subduction zones: South America and the Honshu-Kuril. Though previous workers have inferred trench parallel flow beneath some subduction zones, this was largely based on map views of the data which fail to capture variations in splitting due to changes in sampling angles. From our dataset (which considers the geometrical sampling variations in the slab reference frame) we do not see compelling evidence to prefer the trench parallel model for any particular subduction zone system.

4.2.2. 0 to 50 km deep sources

Measurements from events shallower than 50 km show a slightly different pattern with an average slab-normal ϕ_{slab} detected on rays around azimuth $-60°$ and takeoff angle $60°$ from the strike and dip of the slab respectively (Figs 6 and 7). Note that these measurements appear parallel to the subduction zone trench when viewed in the geographical reference frame (Fig S9). This suggests the existence of a distinct region of anisotropy in the upper ~ 50 km (and therefore within the lithospheric slab). No model perfectly replicates the splitting pattern over the whole range of angles. Though any signal from the shallow anisotropic region would be contaminated by anisotropy in deeper regions obscuring its true nature; therefore we cannot directly compare models with the data. With that caveat, it is interesting to note that the slab normal ϕ_{slab} observations around azimuth $-60°$ and takeoff angle $60°$ are consistent with the pattern expected from the HTI strike parallel model (Fig S23 C); alternatively, a tilting of the slow symmetry axis model (Fig 4 D) so that the axis points down the dip vector of the slab would also produce this pattern. Faults within the slab would be expected to create an SPO fabric that would fit the data reasonably well (Fig S24).

4.2.3. 250 to 550 km deep sources

Fast directions, ϕ_{slab}, from sources in the depth range 250–550 km are not neatly compatible with any of the candidate models considered in Figure S25. There is an approximate fit to the TTI model that we favour to explain the shallower 50–250 km source depth data (Fig S25 D). This may

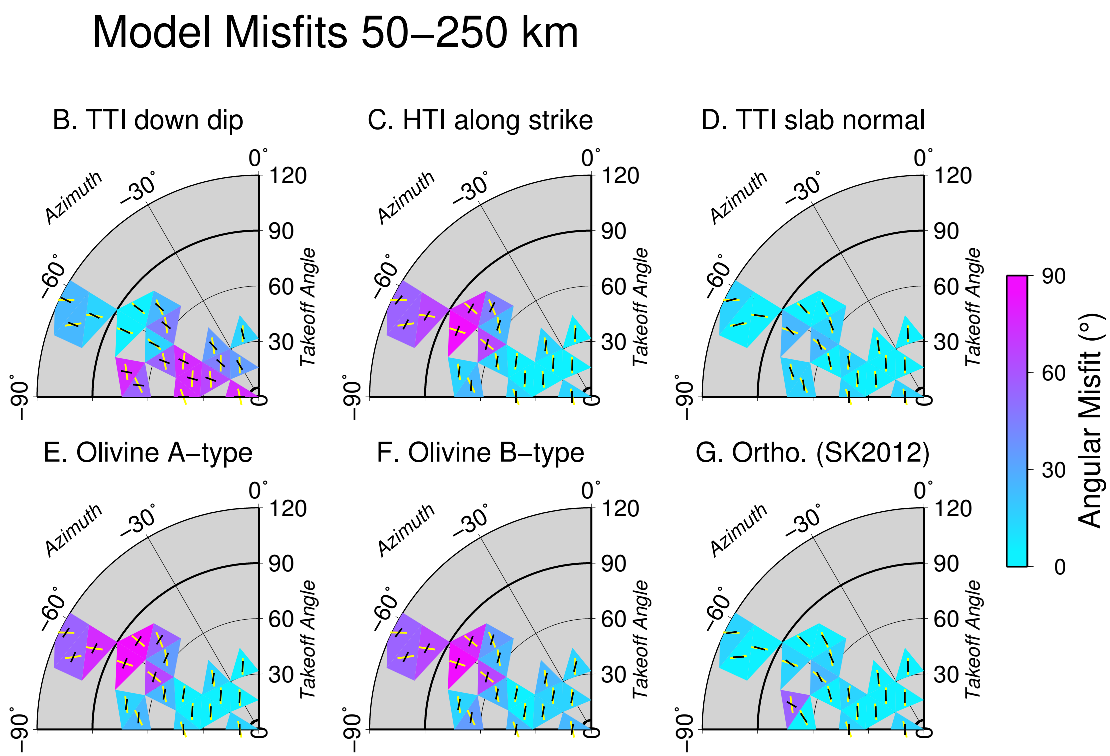

Figure 8: Comparison of averaged ϕ_{slab} observations (from sources in the depth range 50 to 250 km, Fig 7) to the predictions of models in Figure 4 (hence labels start from B). This depth range most directly probes anisotropy in the asthenospheric sub-slab mantle. *Black ticks* show the predicted orientation of ϕ_{slab} according to the model; *yellow ticks* the observed measurement; background colour indicates the angular misfit between these two orientations: cyan colours indicate good fit while magenta colours indicate poor fit. Model B (TTI with symmetry axis pointing down dip of the slab, analogue for olivine A-type under entrained flow,) strongly misfits the data at azimuths normal to the slab though is more compatible at oblique angles. Model C (HTI with symmetry axis pointing along strike, analogue for olivine A-type under trench parallel flow,) fits well for rays with azimuths close to slab normal but fails at oblique angles. Model D (TTI with symmetry axis pointing normal to the slab) fits the data well over a wide range of angles. Models E and F are similar to model C; model G is similar to model D. Refer to Figure 4 for more detailed information about the models.

hint that the above layer extends to deeper depths and misfit is caused by increasing interference with deeper regions of anisotropy. However, if these measurements are sensitive to more than one layer of anisotropy then a more complex analysis is required to interpret these results.

4.2.4. Deeper than 550 km sources

Measurements from sources deeper than 550 km, on average, best fit the model of entrained bridgmanite, though only a small amount of coverage is available (Fig S26 H). This model is derived from a texture model simulated at 30 GPa (∼850 km depth) deformed under simple shear with strain of 2.0 and elastic constants calculated at pressure and temperature of 38 GPa and 1500 K (Mainprice et al., 2008). The entrained bridgmanite model predicts that the strength of anisotropy, at the angles sampled in our dataset, is $\sim 2\%$. From this we infer a sheared layer thickness of ~ 180 km (as discussed earlier to explain delay times of ~ 1 s). A recently published experimentally derived model of deformed bridgmanite (Tsujino et al., 2016) fits the data very well Fig S27.

4.3. Null Measurements

Null measurements are those with δt below the resolution of the data (~ 0.4 s; note lack of measurements below 0.4 s in the "δt (s)" histogram in Fig S8). The percentage of null measurements in the dataset varies between 50% and 70% tending to increase with source depth (Fig 2 C). The large percentage of null measurements requires some explanation. It is important to recognise that these observations do not necessarily imply an isotropic region. Null measurements can occur for a number of reasons:

- because anisotropy is locally very weak or isotropic;
- the wave is sampling along an isotropic direction (e.g., the symmetry axis of a transverse isotropic medium);
- the wave is polarised in the fast or slow direction;
- multiple regions of anisotropy cancel one another out.

The most noteworthy feature of the *null* measurements is that their occurrence depends strongly on the ray takeoff angle in the slab reference frame (Fig 9). Rays sourced in the upper 350 km (excluding the shallowest 50 km) yield fewer null measurements (as a percentage) when propagating down the dip vector of the slab than when travelling normal to the slab plane (Fig 7 B). This may be due to the heterogeneity of the slab itself or it may be due to the style of anisotropy. A TTI medium with symmetry axis pointing normal to the slab could explain this observation because waves travelling down the symmetry axis of such a medium would not split. A TTI model can thus explain both the patterns in null concentrations and the fast directions.

The opposite dependence of null measurements on ray takeoff angle is true for deeper sourced rays (sourced deeper than 350 km): rays propagating down the dip vector of the slab yield more null measurements than those travelling at angles offset from this axis (Fig 9). It is possible that the slab itself provides an (apparently) isotropic pathway in the deep mantle. Alternatively this could be explained by a TTI medium with symmetry axis pointing in the slab dip direction. Note, however, that the favoured entrained bridgmanite model (Fig 4 H) does not predict this observed pattern in null measurements: it predicts reasonably strong splitting for rays travelling in the down slab dip direction. However, all rays in the dataset that propagate down the slab are derived from sources shallower than 550 km (Fig 7 B). This feature cannot therefore be ascribed with confidence to anisotropy in the upper lower mantle (below 660 km –where bridgmanite exists); it allows the possibility that two-layer interference between a lower transition zone layer (in the depth range 550–660 km) and the upper lower mantle gives rise to the abundance of null measurements seen at this angle – this would require that the two layers systematically cancel one-another out.

5. Conceptual Model

A conceptual model of anisotropy beneath a subduction zone inferred from the key features of the dataset is presented in the cartoon of Figure 10. Here we discuss how our observations justify that model followed by a discussion of the possible causes of anisotropy. Working downwards with depth, our conceptual model consists of the following regions of anisotropy:

1. Lithosphere: Despite a wealth of data from shallow events the interpretation of anisotropy in the lithosphere is apparently compromised by interference in the signal from anisotropy in the deeper mantle. Nevertheless a change in fast direction observed with change in source depth – above and below 50 km – indicates the presence of a distinct lithospheric region of anisotropy. Shallow sourced measurements tend to appear parallel to the subduction zone trench when viewed in the geographical reference frame, suggesting that previous reports of widespread trench parallel anisotropy may be biased by the great number of shallow events. The fact that this signal is unique to shallow source data

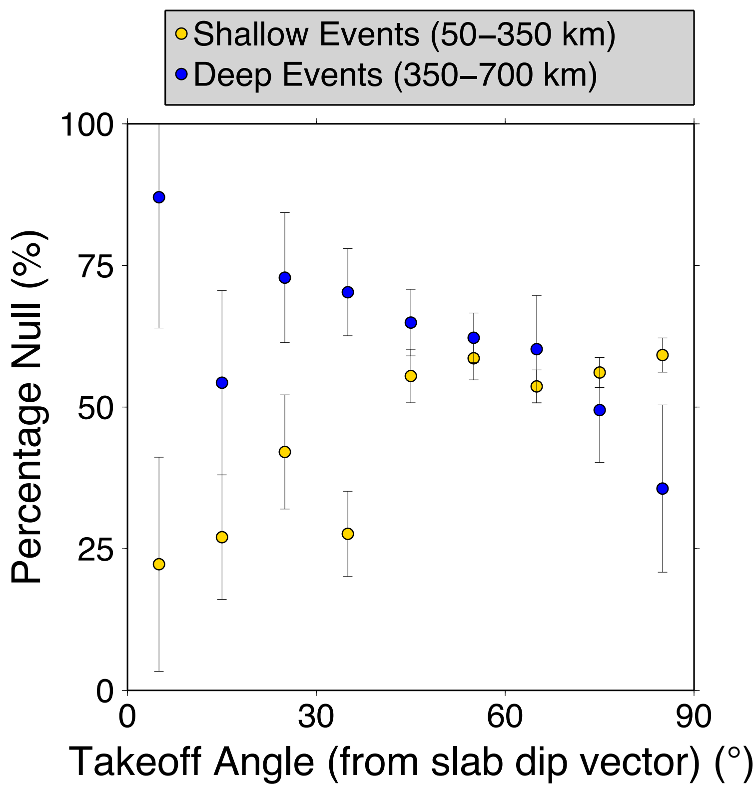

Figure 9: Percentage of null measurements as a function of ray takeoff angle (measured from slab dip vector). Data are divided into shallow (50–350 km, yellow) and deep sources (350–700 km, blue). Error bars are one standard deviation of 1000 untrimmed bootstrap samples (Efron and Tibshirani, 1991). We note the percentage of null measurements increases with takeoff angle for shallow sources and decreases with takeoff angle for deep sources.

(shallower than 50 km depth) implies that this anisotropy does not survive deep subduction.

2. Asthenosphere: The steady reduction in δt with increasing source depth is strong evidence for the presence of anisotropy in the upper ∼200 km. Assuming 2% anisotropy and dipping layer geometry the anisotropic layer thins from 290 km near the surface to 225 km upon subduction to depths beyond ∼ 200 km. Alternatively the strength of anisotropy weakens with depth. In either case we infer that this layer may exist to depths in excess of 400 km. The pattern in ϕ_{slab} strongly resembles that expected from a TTI medium (Fig 8 D) with a slow symmetry axis pointing subnormal to the plane of the subducting slab. Moreover the concentration of null measurements increases as rays propagate closer to this proposed symmetry axis (as expected for a TTI medium). These results are compatible with the strong radial anisotropy model of Song and Kawakatsu (2012).

The previous study of Lynner and Long (2014b) employed similar methodology to this study but came to different conclusions concerning the validity of the strong radial anisotropy model of Song and Kawakatsu (2012). They found the model to be broadly incompatible with their data. Instead they favoured an age dependent model whereby systems with young lithosphere exhibit splitting aligned with absolute plate motion and systems with older lithosphere ($>$ 95 Ma) exhibit splitting parallel to the subduction zone trench. Evidence that our results differ from those of Lynner and Long (2014b) comes from inspecting histograms of ϕ_{slab} misfit from trench parallel: in our study the histogram shows more ‘trench-parallel’ results (Fig 2 B) than the corresponding histogram in their study (their Fig 4 A); though neither study shows a particularly strong dependence of fast direction on the trench orientation. Differences between the two studies may arise due to differences in data coverage and methodology. Our conclusions may also differ due to our use of the slab reference frame in the analysis stage.

3. Transition zone: A lack of depth dependence on δt from sources in the depth range 250–550 km is compatible with isotropy in this depth range. However, we do not conclude that the transition zone is isotropic as the interference between multiple regions of anisotropy could also explain this observation. Interpretation in this depth range is compromised by a paucity of data and the potential for interference between multiple regions of anisotropy, therefore we resist commenting further.

4. Upper lower mantle: Splitting observed on events deeper than 660 km is strong evidence for the presence of anisotropy in the upper lower mantle. To explain the observed δt values of $\sim$ 1 s requires a layer of 2% anisotropy $\sim$ 180 km thick. On average ϕ_{slab} is parallel to the dip direction of the slab resembling a TTI style of anisotropy with fast symmetry axis pointing in the slab dip direction. Furthermore, the concentration of null measurements increases as rays propagate closer to the slab dip direction, as would be expected for this style of anisotropy.

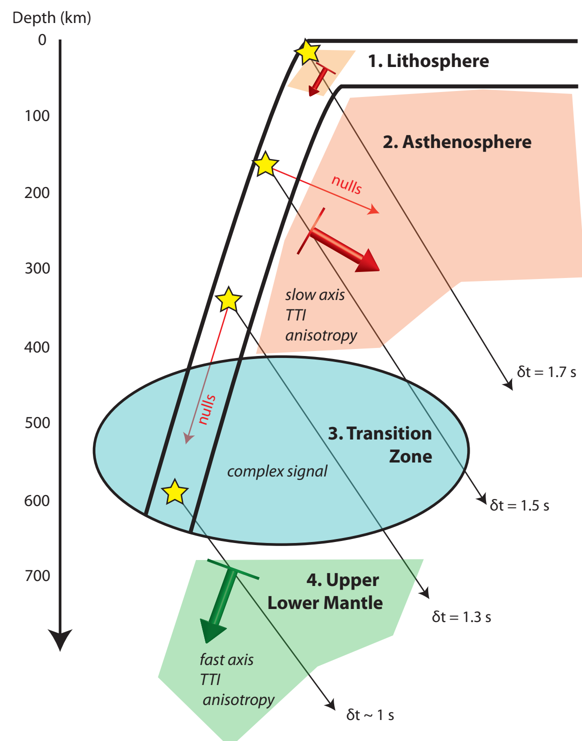

Figure 10: Conceptual model of anisotropy in the sub-slab mantle. **1. Lithosphere:** unusually high frequency of trench parallel observations from sources in upper 50 km, possibly caused by SPO of trench parallel faults, though interference expected from deeper layers clouds interpretation. **2. Asthenosphere:** dependence on fast direction with takeoff angle and azimuth relative to dip and strike of the slab is consistent with that expected from a TTI medium with slow symmetry axis pointing subnormal to the slab. Null measurements are more frequently made on rays travelling along the proposed symmetry axis. Median delay times decline gradually with source depth from ~ 1.7 s for shallower events (50 km depth) to ~ 1.3 s for deeper events (250 km). **3. Transition Zone:** no clearly distinct signal is detected from events in the depth range 250–550 km; this may be because the number of data from this range is low, or that the signal is contaminated by the interference of multiple regions of anisotropy. It is interesting that null measurements become more frequent for rays that shoot down the slab. **4. Upper Lower Mantle:** median delay times ~ 1 s from very deep events evidence the presence of anisotropy in the upper lower mantle; dependence on fast direction with ray angle, and the elevated occurrence of null measurements down the slab, is consistent with TTI medium with fast symmetry axis pointing subparallel to the slab dip direction.

5.1. Possible causes of anisotropy

Anisotropy can be caused by the lattice-preferred orientation (LPO) of intrinsically anisotropic crystals and/or the shape-preferred orientation (SPO) of elastically heterogeneous features of length scale several times shorter than the seismic wavelength. Here we consider the geophysically plausible causes of anisotropy within the regions of our conceptual model (Fig 10):

1. Lithosphere: A simple SPO model of faults in the slab dipping 60° towards the back arc can potentially explain the wealth of dip-normal ϕ_{slab} observations (Fig S24). Such faults are expected to form by flexure of the lithosphere upon subduction. Anisotropy of this type might be enhanced by the addition of LPO from highly anisotropic hydrous phases such as antigorite and talc (Faccenda et al., 2008). Fossil anisotropy in the lithosphere — due to the LPO of olivine crystals in the direction of plate motion during formation (e.g., Shearer and Orcutt, 1986; Tommasi, 1998) — does not explain our observations because this fossil direction does not systematically align parallel to the trench of the subduction zone (Long and Silver, 2008).
2. Asthenosphere: Anisotropy in the peridotitic asthenosphere has widely been considered to be caused by the LPO of olivine crystals with *a* axes oriented in the shear direction by dislocation creep deformation (e.g., Nicolas and Christensen, 1987). The resultant A-type fabric explains the widespread azimuthal anisotropy observed in surface wave studies (e.g., Debayle et al., 2005) and shear wave splitting on SKS phases (e.g., Walpole et al., 2014); such fabrics can also potentially explain the observed radial anisotropy (Becker et al., 2008). Other types of

fabric are possible and may be present (e.g., Karato et al., 2008). Fabrics with strong radial anisotropy are predicted if deformation occurs in the presence of partial melt in the diffusion creep deformation regime (Holtzman et al., 2003; Miyazaki et al., 2013). Fabrics with strong radial anisotropy are also predicted if the medium undergoes axial shortening in the vertical direction (Tommasi et al., 1999). Alternatively an SPO mechanism might explain the strong radial anisotropy. For example horizontal layers of partial melt could contribute radial anisotropy under 'normal' oceanic conditions (Kawakatsu et al., 2009); however, as noted by Song and Kawakatsu (2012), upon subduction any melt is likely to solidify and thereby reduce the strength of this anisotropy. It remains to be determined whether the anisotropy we detect is formed in the ambient asthenosphere and is tilted in place by subduction (implying strong coupling between lithosphere and asthenosphere; Song and Kawakatsu, 2012) or whether it is created by the subduction process itself.

3. Transition zone: Given the potential difficulties in confidently interpreting transition zone anisotropy from our dataset we do not comment on the possible causes of anisotropy. However, previous work has suggested the presence of hydrous phases in this region can explain the anisotropy (Nowacki et al., 2015), and our results are broadly compatible with this interpretation.

4. Upper lower mantle: Bridgmanite is volumetrically the most important mineral, comprising about 70% of the mantle at shallow lower mantle depths; this mineral is strongly anisotropic ($\sim$ 12% shear wave

anisotropy at 660 km depth; Karki, 1999) and is capable of forming LPO fabric (Cordier et al., 2004; Wenk et al., 2004). Theoretical work suggests that the LPO of bridgmanite produces moderate anisotropy ($\sim 2-3\%$ at 38 GPa or $\sim$ 980 km depth; which would likely be stronger at shallower depths; Mainprice et al., 2008). Alternatively an SPO mechanism would require tubule (cigar shaped) inclusions elongated in the dip direction, these inclusions would likely need to be low velocity in order to produce sufficiently strong anisotropy (Kendall and Silver, 1998).

6. Conclusions

In this study we use automation to process a large volume of source-side splitting data on teleseismic S phases. A new method is introduced to propagate uncertainty in the receiver correction into the error of our measurements; and a novel null identification method is employed to aid interpretation. Manually verified quality control reduces the dataset to 6369 high quality measurements made from subduction zone earthquake sources. These data place constraints on the mineralogy and geodynamics of the sub-slab mantle.

We find that the asthenospheric sub-slab mantle is approximately transversely isotropic with a slow symmetry axis pointing subnormal to the plane of the slab (as recently hypothesized; Song and Kawakatsu, 2012). Assuming 2% strength the anisotropic layer is $\sim$ 300 km thick and thins to $\sim$ 200 km upon subduction. Alternatively the fabric strength weakens with depth. In either case we infer the subduction of this fabric to transition zone depths.

Either strong radially anisotropic fabric developed in the asthenosphere under 'normal' conditions is tilted by the subduction process and carried down to transition zone depths or the fabric is created by the subduction process itself. Strong radially anisotropic fabrics in peridotite can be created by axial shortening in the vertical direction, or diffusion creep deformation in the presence of partial melt; fabric created by dislocation creep in olivine might also produce sufficient radial anisotropy, though we do not have sufficient coverage at the necessary angles to detect the expected azimuthal anisotropy in this case. Our results are incompatible with previously suggested models involving trench parallel flow, raising doubt over its widespread occurrence.

An abundance of 'trench parallel' splitting is measured on the shallowest data (from sources in the upper 50 km) suggesting a unique style of anisotropy contained in the slab. This anisotropy could be caused by the shape preferred orientation of faults formed parallel to the trench by slab bending.

The upper lower mantle appears approximately transversely isotropy with a fast symmetry axis pointing subparallel to the subduction direction. Assuming 2% strength the anisotropic layer is ~ 200 km thick. The deformation of bridgmanite is a plausible candidate mechanism to explain our observations.

7. Acknowledgements

The research leading to these results has received funding from the European Research Council under the European Unions Seventh Framework Program (FP7/20072013)/ERC grant agreement 240473 CoMITAC. We thank Andy Nowacki for helpful discussions particularly with regards to rotating the data into the slab reference frame. We also thank two anonymous reviewers for helpful comments that improved the manuscript. This work would not have been possible without the IRIS DMC data archive. Figures were mostly produced using the free Generic Mapping Tools software (GMT) (Wessel and Smith, 1991).

Alisic, L., Gurnis, M., Stadler, G., 2012. Multi-scale dynamics and rheology of mantle flow with plates. Journal of geophysical Research 117 (B10402).

Ando, M., Ishikawa, Y., Wada, H., Jul. 1980. S-wave anisotropy in the upper mantle under a volcanic area in Japan. Nature 286, 43–46.

Becker, T. W., Faccenna, C., 2009. A Review of the Role of Subduction Dynamics for Regional and Global Plate Motions. In: Subduction Zone Geodynamics. Frontiers in earth sciences, Berlin, Heidelberg, pp. 3–34.

Becker, T. W., Kustowski, B., Ekstrom, G., 2008. Radial seismic anisotropy as a constraint for upper mantle rheology. Earth Planet. Sci. Lett.

Ben Ismail, W., Mainprice, D., Oct. 1998. An olivine fabric database: an overview of upper mantle fabrics and seismic anisotropy. Tectonophysics 296 (1-2), 145–157.

Bercovici, D., 2003. The generation of plate tectonics from mantle convection. Earth Planet. Sci. Lett.

Billen, M. I., 2008. Modeling the dynamics of subducting slabs. Annu. Rev. Earth Pl. Sc.

Civello, S., 2004. Toroidal mantle flow around the Calabrian slab (Italy) from SKS splitting. Geophys. Res. Lett. 31 (10), L10601.

Cordier, P., Ungár, T., Zsoldos, L., Tichy, G., Apr. 2004. Dislocation creep in $MgSiO_3$ perovskite at conditions of the Earth's uppermost lower mantle. Nature 428 (6985), 837–840.

Debayle, E., Kennett, B., Priestley, K., 2005. Global azimuthal seismic anisotropy and the unique plate-motion deformation of Australia. Nature 433, 509–512.

Di Leo, J. F., Walker, A. M., Li, Z. H., Wookey, J., Ribe, N. M., Kendall, J. M., Tommasi, A., 2014. Development of texture and seismic anisotropy during the onset of subduction. Geochem. Geophys. Geosyst. 15 (1).

Di Leo, J. F., Wookey, J., Hammond, J. O. S., Kendall, J. M., Kaneshima, S., Inoue, H., Yamashina, T., Harjadi, P., 2012. Deformation and mantle flow beneath the Sangihe subduction zone from seismic anisotropy. Phys. Earth Planet. Int. 194, 38–54.

Dziewonski, A. M., Anderson, D. L., 1981. Preliminary reference Earth model. Phys. Earth Planet. Int. 25 (4), 297–356.

Efron, B., Tibshirani, R., 1991. Statistical data analysis in the computer age. Science 253 (5018), 390–395.

Faccenda, M., Burlini, L., Gerya, T. V., Mainprice, D., Oct. 2008. Fault-induced seismic anisotropy by hydration in subducting oceanic plates. Nature 455 (7216), 1097–1100.

Faccenda, M., Capitanio, F. A., 2012. Development of mantle seismic anisotropy during subduction-induced 3-D flow. Geophys. Res. Lett. 39 (L11305).

Fischer, K. M., Wiens, D. A., Jul. 1996. The depth distribution of mantle anisotropy beneath the Tonga subduction zone. Earth Planet. Sci. Lett. 142 (1-2), 253–260.

Fouch, M., Fischer, K., 1996. Mantle anisotropy beneath northwest Pacific subduction zones. J. Geophys. Res. 101 (B7), 15987–16002.

Hayes, G. P., Wald, D. J., Johnson, R. L., Jan. 2012. Slab1.0: A three-dimensional model of global subduction zone geometries. J. Geophys. Res. 117 (B01302).

Holtzman, B. K., Kohlstedt, D. L., Zimmerman, M. E., Heidelbach, F., Hiraga, T., Hustoft, J., Aug. 2003. Melt Segregation and Strain Partitioning: Implications for Seismic Anisotropy and Mantle Flow. Science 301 (5637), 1227–1230.

Honda, S., 2009. Numerical simulations of mantle flow around slab edges. Earth Planet. Sci. Lett. 277, 112–122.

Houser, C., Masters, G., Shearer, P., Laske, G., 2008. Shear and compressional velocity models of the mantle from cluster analysis of long-period waveforms. Geophys. J. Int. 174, 195–212.

Jung, H., Katayama, I., Jiang, Z., Hiraga, T., Karato, S., Jul. 2006. Effect of water and stress on the lattice-preferred orientation of olivine. Tectonophysics 421 (1-2), 1–22.

Jung, H., Mo, W., Green, H. W., Jan. 2009. Upper mantle seismic anisotropy resulting from pressure-induced slip transition in olivine. Nature Geosci. 2 (1), 73–77.

Kaneshima, S., 2014. Upper bounds of seismic anisotropy in the Tonga slab near deep earthquake foci and in the lower mantle. Geophys. J. Int.

Kaneshima, S., Silver, P. G., Dec. 1992. A search for source side mantle anisotropy. Geophys. Res. Lett. 19 (10), 1049–1052.

Karato, S., Jung, H., Katayama, I., Skemer, P., May 2008. Geodynamic Significance of Seismic Anisotropy of the Upper Mantle: New Insights from Laboratory Studies. Annu. Rev. Earth Pl. Sc. 36 (1), 59–95.

Karki, B. B., Nov. 1999. First-Principles Determination of Elastic Anisotropy and Wave Velocities of MgO at Lower Mantle Conditions. Science 286 (5445), 1705–1707.

Kawakatsu, H., Kumar, P., Takei, Y., Shinohara, M., Kanazawa, T., Araki, E., Suyehiro, K., 2009. Seismic Evidence for Sharp Lithosphere-Asthenosphere Boundaries of Oceanic Plates. Science 324 (5926), 499–502.

Kendall, J. M., Silver, P. G., 1998. Investigating causes of D″ anistropy. In: The core-mantle boundary region. American Geophysical Union, Washington, D. C., pp. 97–118.

Kincaid, C., 1995. Subduction dynamics: From the trench to the coremantle boundary. Rev. Geophys. 33 (S1), 401–412.

Kincaid, C., Griffiths, R. W., Sep. 2003. Laboratory models of the thermal evolution of the mantle during rollback subduction. Nature 425 (6953), 58–62.

Lee, J., Jung, H., Jan. 2015. Lattice-preferred orientation of olivine found in diamond-bearing garnet peridotites in Finsch, South Africa and implications for seismic anisotropy. Journal of Structural Geology 70, 12–22.

Li, Z. H., Di Leo, J. F., Ribe, N. M., 2014. Subductioninduced mantle flow, finite strain, and seismic anisotropy: Numerical modeling. J. Geophys. Res. 119 (6), 5052–5076.

Long, M. D., Silver, P. G., 2008. The subduction zone flow field from seismic anisotropy: a global view. Science 319, 315–319.

Long, M. D., Silver, P. G., 2009. Mantle flow in subduction systems: The subslab flow field and implications for mantle dynamics. Journal of geophysical Research 114 (B10312).

Lowman, J. P., Pinero-Feliciangeli, L. T., Kendall, J. M., Hosein Shahnas, M., 2007. Influence of convergent plate boundaries on upper mantle flow and implications for seismic anisotropy. Geochem. Geophys. Geosyst. 8 (Q08007).

Lynner, C., Long, M. D., Jan. 2013. Sub-slab seismic anisotropy and mantle flow beneath the Caribbean and Scotia subduction zones: Effects of slab morphology and kinematics. Earth Planet. Sci. Lett. 361, 367–378.

Lynner, C., Long, M. D., May 2014a. Subslab anisotropy beneath the Sumatra and circum-Pacific subduction zones from source-side shear wave splitting observations. Geochem. Geophys. Geosyst. 15.

Lynner, C., Long, M. D., 2014b. Testing models of sub-slab anisotropy using a global compilation of source-side shear wave splitting data. J. Geophys. Res. 119, 7226–7244.

Lynner, C., Long, M. D., 2015. Heterogeneous seismic anisotropy in the transition zone and uppermost lower mantle: evidence from South America, Izu-Bonin and Japan. Geophys. J. Int.

Mainprice, D., Tommasi, A., Ferré, D., Carrez, P., Cordier, P., Jul. 2008. Predicted glide systems and crystal preferred orientations of polycrystalline silicate Mg-Perovskite at high pressure: Implications for the seismic anisotropy in the lower mantle. Earth Planet. Sci. Lett. 271 (1-4), 135–144.

Meade, C., Silver, P. G., Kaneshima, S., 1995. Laboratory and Seismological Observations of Lower Mantle Isotropy. Geophys. Res. Lett. 22 (10), 1293–1296.

Miyazaki, T., Sueyoshi, K., Hiraga, T., Oct. 2013. Olivine crystals align during diffusion creep of Earth's upper mantle. Nature 502 (7471), 321–326.

Mohiuddin, A., Long, M. D., Lynner, C., Aug. 2015. Mid-mantle seismic anisotropy beneath southwestern Pacific subduction systems and implications for mid-mantle deformation. Phys. Earth Planet. Int. 245, 1–14.

Nettles, M., Dziewonski, A. M., 2008. Radially anisotropic shear velocity structure of the upper mantle globally and beneath North America. J. Geophys. Res. 113 (B02303).

Nicolas, A., Christensen, N. I., 1987. Formation of anisotropy in upper mantle peridotites: A review. Composition.

Nowacki, A., Kendall, J. M., Wookey, J., Feb. 2012. Mantle anisotropy beneath the Earth's mid-ocean ridges. Earth Planet. Sci. Lett. 317-318, 56–67.

Nowacki, A., Kendall, J. M., Wookey, J., Pemberton, A., Feb. 2015. Mid-mantle anisotropy in subduction zones and deep water transport. Geochem. Geophys. Geosyst. 16, 764–784.

Ohuchi, T., Kawazoe, T., Nishihara, Y., Nishiyama, N., Irifune, T., Apr. 2011. High pressure and temperature fabric transitions in olivine and variations in upper mantle seismic anisotropy. Earth Planet. Sci. Lett. 304 (1-2), 55–63.

Paczkowski, K., Montési, L., Long, M. D., Thissen, C. J., 2014. Three-dimensional flow in the subslab mantle. Geochem. Geophys. Geosyst. 15, 3989–4008.

Panning, M., Romanowicz, B., 2006. A three-dimensional radially anisotropic model of shear velocity in the whole mantle. Geophys. J. Int. 167 (1), 361–379.

Parzen, E., 1962. On Estimation of a Probability Density Function and Mode. The Annals of Mathematical Statistics.

Phipps Morgan, J., Hasenclever, J., Hort, M., Rüpke, L., Parmentier, E. M., Jun. 2007. On subducting slab entrainment of buoyant asthenosphere. Terra Nova 19 (3), 167–173.

Restivo, A., Helffrich, G., 1999. Teleseismic shear wave splitting measurements in noisy environments. Geophys. J. Int. 137, 821–830.

Ribe, N., 1992. On the relation between seismic anisotropy and finite strain. J. Geophys. Res. 97 (B6), 8737–8747.

Ribe, N. M., 1989. Seismic anisotropy and mantle flow. J. Geophys. Res. 94 (B4), 4213–4223.

Russo, R., Silver, P. G., 1994. Trench-parallel flow beneath the Nazca plate from seismic anisotropy. Science 263 (5150), 1105–1111.

Savage, M., 1999. Seismic anisotropy and mantle deformation: What have we learned from shear wave splitting? Rev. Geophys. 37 (1), 65–106.

Shearer, P. M., Orcutt, J. A., Dec. 1986. Compressional and shear wave anisotropy in the oceanic lithosphere - the Ngendei seismic refraction experiment. Geophys. J. Int. 87 (3), 967–1003.

Silver, P. G., Chan, W., Sep. 1991. Shear Wave Splitting and Subcontinental Mantle Deformation. J. Geophys. Res. 96 (B10), 16429–16454.

Song, T., Kawakatsu, H., 2012. Subduction of oceanic asthenosphere: Evidence from sub-slab seismic anisotropy. Geophys. Res. Lett. 39 (L17301).

Song, T.-R. A., Kawakatsu, H., Apr. 2013. Subduction of oceanic asthenosphere: A critical appraisal in central Alaska. Earth Planet. Sci. Lett. 367, 82–94.

Tandon, G. P., Weng, G. J., Oct. 1984. The effect of aspect ratio of inclusions on the elastic properties of unidirectionally aligned composites. Polym. Compos. 5 (4), 327–333.

Teanby, N., Kendall, J. M., Van der Baan, M., 2004. Automation of shear-wave splitting measurements using cluster analysis. Bull. Seis. Soc. Am. 94 (2), 453–463.

Thomsen, L., 1986. Weak Elastic Anisotropy. Geophysics 51 (10), 1954–1966.

Tommasi, A., Jul. 1998. Forward modeling of the development of seismic anisotropy in the upper mantle. Earth Planet. Sci. Lett. 160 (1-2), 1–13.

Tommasi, A., Tikoff, B., Vauchez, A., Apr. 1999. Upper mantle tectonics: three-dimensional deformation, olivine crystallographic fabrics and seismic properties. Earth Planet. Sci. Lett. 168 (1-2), 173–186.

Trampert, J., van Heijst, H., May 2002. Global Azimuthal Anisotropy in the Transition Zone. Science 296 (5571), 1297–1299.

Tsujino, N., Nishihara, Y., Yamazaki, D., Seto, Y., Higo, Y., Takahashi, E., Oct. 2016. Mantle dynamics inferred from the crystallographic preferred orientation of bridgmanite. Nature.

Vinnik, L. P., Kind, R., 1993. Ellipticity of Teleseismic S-Particle Motion. Geophys. J. Int. 113, 165–174.

Walpole, J., Wookey, J., Masters, G., Kendall, J. M., Apr. 2014. A uniformly processed dataset of SKS shear wave splitting measurements: A global investigation of upper mantle anisotropy beneath seismic stations. Geochem. Geophys. Geosyst. 15.

Wenk, H. R., Lonardeli, I., Pehl, J., Devine, J., 2004. In situ observation of texture development in olivine, ringwoodite, magnesiowüstite and silicate perovskite at high pressure. Earth Planet. Sci. Lett. 226, 507–519.

Wessel, P., Smith, W. H. F., 1991. Free software helps map and display data. Eos Trans. AGU 72 (41), 441–448.

Wolfe, C. J., Silver, P. G., 1998. Seismic anisotropy of oceanic upper mantle: Shear wave splitting methodologies and observations. Journal of geophysical Research 103 (B1), 749–771.

Wookey, J., Kendall, J. M., 2004. Evidence of midmantle anisotropy from shear wave splitting and the influence of shear-coupled P waves. J. Geophys. Res. 109 (B7), B07309.

Wookey, J., Kendall, J. M., 2008. Constraints on lowermost mantle mineralogy and fabric beneath Siberia from seismic anisotropy. Earth Planet. Sci. Lett. 275 (1-2), 32–42.

Wookey, J., Kendall, J. M., Barruol, G., 2002. Mid-mantle deformation inferred from seismic anisotropy. Nature 415, 777–780.

Wookey, J., Kendall, J. M., Rumpker, G., 2005. Lowermost mantle anisotropy beneath the north Pacific from differential S-ScS splitting. Geophys. J. Int. 161 (3), 829–838.

Wuestefeld, A., Al-Harrasi, O., Verdon, J. P., Wookey, J., Kendall, J. M., 2010. A strategy for automated analysis of passive microseismic data to image seismic anisotropy and fracture characteristics. Geophys. Prosp. 58, 755–773.

Wuestefeld, A., Bokelmann, G., 2007. Null detection in shear-wave splitting measurements. Bull. Seis. Soc. Am. 97 (4), 1204–1211.

Yuan, K., Beghein, C., Jul. 2013. Seismic anisotropy changes across upper mantle phase transitions. Earth Planet. Sci. Lett. 374, 132–144.

Zandt, G., Humphreys, E., 2008. Toroidal mantle flow through the western U.S. slab window. Geology 36 (4), 295–298.